Simulation of the Effect of Cable Indent Shape on the Shear Behavior of Concrete-Cable Interaction Surface using PFC2D

V. Sarfarazi

Dept. of Mining, Hamedan University of Technology, Iran

* Corresponding Author: *vahab.sarfarazi@gmail.com*
(Received: April 2020, Accepted:January 2021)

Keywords	Abstract
Shear Strength **Indent Shape** **Concrete Bolt** **PFC2D**	In this paper, the effect of cable indent shape on the shear behavior of concrete-cable attachment surface has been investigated using PFC2D. Firstly, calibration of PFC was performed using the Brazilian experimental test and uniaxial compression test to reproduce the concrete sample. After calibration of PFC2D, punch shear tests were simulated by creating a rectangular concrete model in PFC2D. Numerical models with a dimension of 100mm

*100 mm were prepared. cable with different indent shape was inserted within the model. The punch shear test condition was added to the model. The normal load was fixed at 3.7 MPa ($\sigma_c/10$) and shear load was applied to the model till failure occurred. The results show that tensile cracks are the dominant mode of failure that occurs in the attachment surface. Also, the shape of the attachment surface has an important effect on the failure mechanism of concrete. The shear strength increased by increasing both of the bolt indent width and length.

1. INTRODUCTION

Cables play an important role in strengthening the surrounding concrete, limiting the dislocation or slip between blocks, and effectively improving the stability of concrete engineering structures. Among all types, the full-length bonded bolts have been widely used in various underground engineering projects [1, 2]. Significant achievements have been made in the study of bolted jointed concrete, from both experimental and theoretical perspectives. Sten [3] carried out an experimental study on full-length cement mortar bolts embedded in the granite and analyzed the impact of bolts on the shear strength of joints. Gerrard [4] performed an experimental study and a theoretical discussion on the effect of bolts on the shear strength of joints. Spang et al. [5] studied the reinforcement effect of anchor rod in a rock mass with different properties through physical experiments and found that bolts can significantly improve the shear strength of jointed rock mass. Chen et al. [6] investigate the shear behavior of bolted rock joints with different roughness. Direct shear tests

on both bolted and unbolted artificial joint specimens were conducted under various normal stresses. Zhang et al. [7] proposed the roughness parameters that considered that the anisotropic characteristic of joint roughness can capture the difference of roughness in forward and reverse directions along a single joint profile. The capacity to resist rock deformation is one of the important parameters affecting the shear strength of bolted jointed rock mass. Pellet and Egger [8] established a new analytical model to predict the contribution of bolts to the shear strength of a rock joint, then compared the performance of this analytical model with experimental results to show its capability, and to describe the observed phenomenon. Ferrero [9] investigated the influence of bolt type on shear strength of rock mass for different rocks. However, there have been few studies on the influence of bolt elongation, bolt strength, and other factors on the reinforcement effect. Particularly given that a systematic study is lacking in evaluating and optimizing the bolted effect in practical engineering. With the advancement of numerical simulation, many scholars have explored the shear failure

mechanism of rocks using different numerical techniques. There are four basic types of numerical methods as used in geomechanics i.e. the finite element method (FEM) [10, 11], the finite difference method (FDM) [12, 13], the direct and indirect boundary element methods (BEMs) [14-17] and the discrete element method (DEM) [18-20].

Liu and Ju [10] used FLAC three-dimensional (3D) to study the influence of pre-stress on the shear behavior of joints. Selvadurai and Yu [11] adopted the finite element method to simulate the joint direct shear tests, and the simulated results were in good agreement with the experimental results. However, the disadvantage of using the continuous medium theory to predict the deformation and failure mechanism of joints during loading is that it is not able to realistically reflect the breaking and weakening effects of rocks and joints. To simulate the rock fracture process, some scholars have used the discrete element method, such as the Particle Flow Code (PFC) to perform the simulations. For example, Bahaaddini et al. [12] proposed a new shear box genesis approach to overcome the unrealistic increase of shear strength and dilation angle in PFC. Zhou et al. [13] modeled the direct shear experiments of rock joints with PFC, and discussed the evolution characteristics and failure mechanism of joints during the direct shear experiment, from both macroscopic and microscopic perspectives. Park and Song [18] examined the influence of geometric characteristics and microscopic properties of joints on the shear performance by using PFC 3D to simulate the direct shear process. As evidenced by these studies, the discrete element method has become important method that has been widely used to study the shear failure of jointed rock. However, when using the discrete element method to study bolted jointed rock, the bolt is often represented by discrete particles. For example, Zhao et al. [19] and others used the PFC software to simulate the interface mechanics of bolt. Although the results are good, the bolt is practically a homogeneous continuous medium, and the realistic mechanical properties of the bolt may be described more accurately by the finite element method. The finite element cohesive model has been widely used in the simulation of cracks in brittle materials, such as crystals and rocks. The CZM (cohesive zone model) was first proposed by Dugdale [20] and Barenblatt [21] in the 1960s, which is different from the traditional finite element model. It focuses more on simulating the microstructure of materials and can describe the discontinuity of brittle materials such as rocks. CZM-FEM has been widely used in engineering. It can describe the bond-slip action between steel rebars and surrounding concrete and the crack propagation of composite material plates [22-24]. The crack tip singularity problem can be avoided by using this method to simulate the crack initiation. Recently, Su et al. [25] developed an algorithm of embedding cohesive elements in solid finite element grids, which allows for fracture simulation of complex structures. The objective of this work is to conduct numerical simulations to explore the shear failure mechanism of bolted rock joints.

2. PFC SOFTWARE

PFC is a discrete element commercial software developed by the Itasca Consulting Group and has been already widely used in the rock mechanics field [26]. PFC2D represents a rock mass as an assemblage of circular disks with a finite thickness and connected via cohesive and frictional bonds. A basic linear contact model describes the elastic relationship between the relative displacements and forces of disks at the point contact, as shown in Figure1. This model involves the contact normal force component, Fn, contact overlap, Un, shear force increment, ΔFs, and shear displacement increment, ΔUs, and is given by

$$F_n = k_n U_n \qquad\qquad (1)$$

Where kn is the normal stiffness at the contact. The value of kn is determined by the current contact stiffness model. Note that the normal stiffness, kn, is a secant modulus in that it relates to total displacement and force. The shear stiffness ks, on the other hand, is a tangent modulus in that it relates incremental displacement and force. An upper case K will be used to denote a secant modulus, and a lower case k will be used to denote a tangent modulus. The computation of the normal contact force from the geometry alone makes the code less prone to numerical drift and able to handle arbitrary placement of balls and changes in ball radii after a simulation has begun. The shear contact force is computed incrementally. When the contact is formed, the total shear contact force is initialized to zero. Each subsequent relative shear displacement increment results in an increment of elastic shear force that is added to the current value. The motion of the contact must be considered during this procedure.
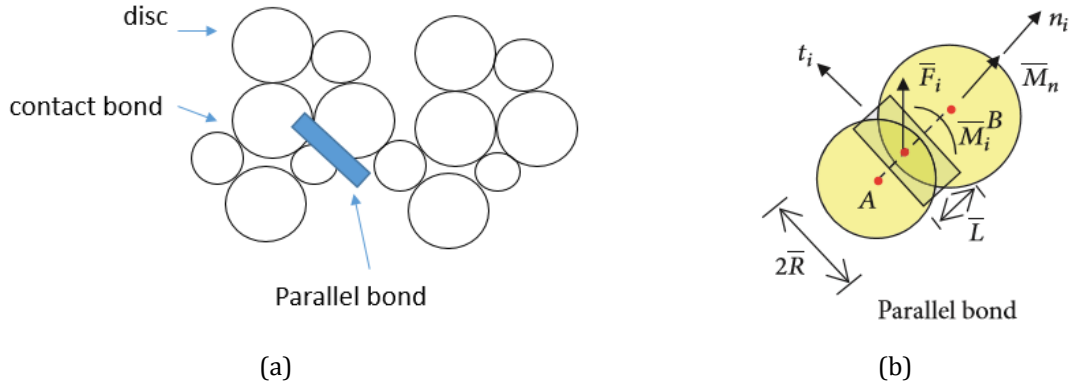
Figure1. The parallel bond model and the stress state between disks [27].

The contact velocity can be resolved into normal and shear components with respect to the contact plane. Denoting these components by V_i^n and V_i^s for the normal and shear components, respectively, the shear component of the contact velocity can be written as

$$V_i^s = V_i - V_i^n = V_i - V_j n_j n_i \qquad (2)$$

The shear component of the contact displacement increment vector, occurring over a time step of Δt, is calculated by

$$\Delta U_i^s = V_i^s \Delta t \qquad (3)$$

which is used to calculate the shear elastic force-increment vector

$$\Delta F_s = -k_s \Delta U_s \qquad (4)$$

The frictional resistance of the contact is given by

$$F_s \leq \mu F_n \qquad (5)$$

where μ is the friction coefficient between the disks. To simulate a relatively brittle rock-like material, it is necessary to cement these disks with a bonded model. This study uses the parallel bond model, which resists not only the contact forces but also the moments between the disks at a cemented contact (Figure1). The function mechanism of the parallel bond model is described by

$$\Delta \bar{F}_n = \bar{k}_n A \Delta U_n$$
$$\Delta \bar{F}_s = \bar{k}_s A \Delta U_s$$
$$\Delta \bar{M}_n = \bar{k}_s J \Delta \theta_n \qquad (6)$$
$$\Delta \bar{M}_s = \bar{k}_n J \Delta \theta_s$$

Where $\bar{F}_n$ and $\bar{F}_s$ are the force components about the center of the cemented-contact zone, $\bar{M}_n$ and $\bar{M}_s$ are the moments about the center of the cemented-contact zone, $\bar{k}_n$ and $\bar{k}_s$ are the normal and shear bond stiffness per unit area, respectively, θn and θs is the rotation angle components, and A, J, and I are the area, polar moment of inertia, and moment of inertia of the

bond contact cross-section, respectively. The strength of the cemented contact is then given by

$$\bar{\sigma}_{max} = -\frac{-\bar{F}_n}{A} + \frac{|\bar{M}_s|\bar{R}}{I} < \bar{\sigma}_c$$
$$\bar{\tau}_{max} = -\frac{-\bar{F}_s}{A} + \frac{|\bar{M}_n|\bar{R}}{J} < \tau_c \qquad (7)$$

Where $\bar{R}$ the radius of the bonded zone between the disks, t is is the length of the bonded zone between the disks (Figure1), and $\bar{\sigma}c$ and $\bar{\tau}c$ are the tensile and shear strength of the bond contact, respectively. Tensile cracks occur when the applied tensile stress exceeds the specified tensile strength of the parallel bond, $\bar{\sigma}c$. Shear cracks occur when the applied shear stress exceeds the specified shear strength of the parallel bond, $\bar{\tau}c$, either by rotation or by the shearing of the disks. The tensile strength at the contact immediately drops to zero once the crack occurs, and the shear strength reduces to the residual friction strength [23,26].

3. PUNCH SHEAR TEST SIMULATION OF THE CABLE USING PFC2D

3.1. Micro parameters of the concrete Sample

The standard process of generating a PFC2D assembly to represent a test model, used in this article, is described in detail by Potyondy and Cundall [27]. The process involves: particle generation, packing the particles, isotropic stress installation (stress initialization), floating particle (floater) elimination, and bond installation. A gravity effect wasn't needed since the specimens were small, and the gravity-induced stress gradient had a negligible effect on the macroscopic behavior. Uniform distribution function was used for particle distribution in the model. The porosity was 0.08%. This value was constant during the calibration process. The software calculates the total area of the model. Then the total area is minus 0.08% of the total surface. The remaining area is divided into the

average area of two discs. In this way, the total number of discs can be generated. After disc generation, the radius of discs was decreased to reach a desired isotropic stress

Uniaxial compressive strength and Brazilian tests were carried out to calibrate the properties of particles and parallel bonds in the bonded particle model (Ghazvinian et al. [28]). Adopting the micro-properties listed in Table1 and the standard calibration procedures (Potyondy and Cundall [27]), a calibrated PFC particle assembly was created for concrete. Fig 2 shows numerical compression test results. The Red line and the black line shows a shear crack and tensile cracks, respectively. As can be seen, tensile cracks develop within the model. This is in accordance with the typical failure pattern that occurred in the experimental test.

Fig 3 a and b shows experimental Brazilian test and numerical simulation, respectively. The results show a well match between the experimental test and numerical simulation. Fig 3 c shows stress versus strain in experimental test and numerical simulations for the uniaxial

test. The results show a well match between experimental test and numerical simulation. Table 2 shows the comparison between mechanical properties rendered by experimental test and numerical simulation. The results show a well match between experimental test and numerical simulation.
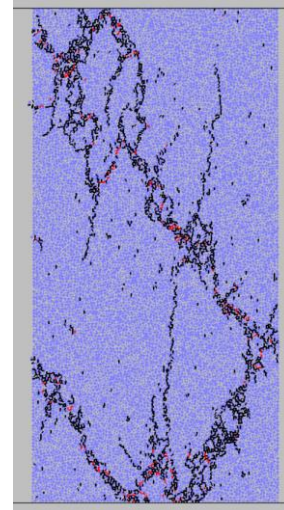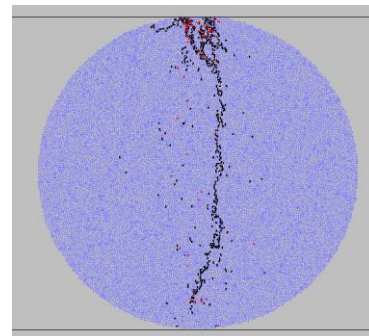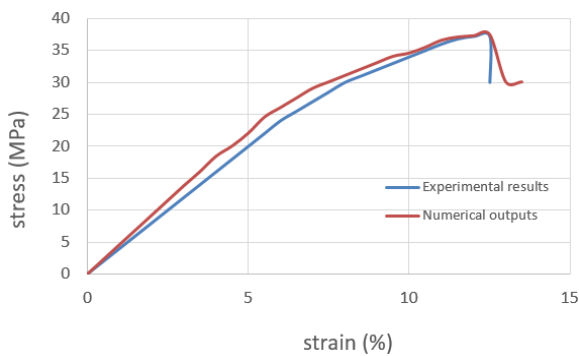

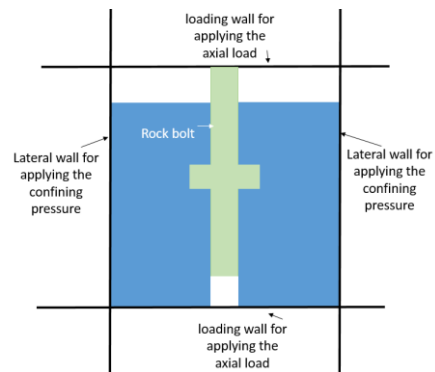**Figure 2. Numerical compression test results**

(a)

(b)

(c)

(d)

Figure 3. failure pattern in a) physical sample, b) PFC2D model, c) compressive stress versus strain, d) schematic view of punch shear test.

Table 1. Micro properties used to represent the concrete

Parameter	Value	Parameter	Value
Type of particle	disc	Parallel bond radius multiplier	1
Density (Kg/m3)	3000	Young modulus of the parallel bond (GPa)	70
Minimum radius (mm)	0.27	Parallel bond stiffness ratio	1.7
Size ratio	1.56	Particle friction coefficient	0.4
Porosity ratio	0.08	Parallel bond normal strength, mean (MPa)	40
Damping coefficient	0.7	Parallel bond normal strength, SD (MPa)	2
Contact young modulus (GPa)	70	Parallel bond shear strength, mean (MPa)	40
Stiffness ratio	1.7	Parallel bond shear strength, SD (MPa)	2

Table 2. Mechanical properties in numerical models and experimental samples.

parameter	Numerical output	Experimental result
Uniaxial compressive strength (MPa)	37.4	37.2
Young modulus (GPa)	19.3	19.1
Tensile strength (MPa)	3.4	3.3

3.2. model preparation using Particle Flow Code

After calibration of PFC2D, punch shear tests were simulated by creating a rectangular concrete model in PFC2D (by using the calibrated micro-parameters). Fig 3d, shows a schematic view of the punch shear test. The PFC specimen had a dimension of 10 cm* 10 cm. One cable with a different indent shape was inserted within the model. cable was created by the clump particle model. The indent dimension were (a*b in Figs 4-7), 5mm*10mm (Fig 4a), 5mm*15mm (Fig 4b), 5mm*20 mm (Fig 4c), 5mm*25mm (Fig 4d), 5*30mm (Fig 4e), 10mm*10mm (Fig 5a), 10mm*15mm (Fig 5b), 10mm*20 mm (Fig 5c), 10mm*25mm (Fig 5d), 10*30mm (Fig 5e), 20mm*10mm (Fig 6a), 20mm*15mm (Fig 6b), 20mm*20 mm (Fig 6c), 20mm*25mm (Fig 6d), 20*30mm (Fig 6e), 30mm*10mm (Fig 7a), 30mm*15mm (Fig 7b), 30mm*20 mm (Fig 7c), 30mm*25mm (Fig 7d) and 30*30mm(Fig 7e). Two vertical bands of the particle were removed from the top and bottom of the model to create the punching shear test condition (Fig 4-7). This leads to isotropic stress redistribution in the model. Whereas deletion of balls numbers are constant in all of the models, therefore their effects are constant on the isotropic stress. The right and left walls apply the confining pressure and the upper wall and lower wall apply shear force. The normal load was fixed at 3.7 MPa ($\sigma c/10$) and shear load was applied to the model till failure occurred. The shear force was registered by taking the reaction forces on the upper wall.

4. NUMERICAL RESULTS

4.1. The effect of bolt indent dimension on the failure pattern of numerical model

Fig 8-11 shows the effect of bolt indent dimension on the failure pattern of the numerical model. The black line and red line are representative of tensile crack and shear crack respectively.

a) bolt length was 5 cm (a in Fig 4a):

When cable width was 10cm (Fig 8a), tensile cracks initiate between the bolt and rock and propagate toward the model edge. When cable width was 15cm (Fig 8b), tensile cracks initiate between the bolt and rock and propagate toward the model edge. In this configuration four tensile wings crack initiate from the tip of the indent and propagate diagonally till coalescence with the bolt-rock interface. When cable width was 20cm (Fig 8c), tensile cracks initiate between the bolt and rock and propagate toward the model edge. In this configuration four tensile wing crack initiate from the tip of the indent and propagate diagonally till coalescence with the bolt-rock interface. When cable width was 25cm (Fig 8d), tensile cracks initiate between the bolt and rock and propagate toward the model edge. In this configuration four tensile wing crack initiate from the tip of the indent and propagate diagonally till coalescence with the bolt-rock interface. When cable width was 30cm (Fig 8e), tensile cracks initiate between the bolt and rock and propagate toward the model edge. In this configuration four tensile wing crack initiate from the tip of the indent and propagate diagonally till coalescence with the bolt-rock interface. Two rock wedges formed in this condition.

b) bolt length was 10 cm (a in Fig 4a):

When cable width was 10cm (Fig 9a), tensile cracks initiate between the bolt and rock and propagate toward the model edge. When cable width was 15cm (Fig 9b), tensile cracks initiate between the bolt and rock and propagate toward the model edge. In this configuration four tensile wing crack initiate from the tip of the indent and propagate diagonally till coalescence with the bolt-rock interface. When cable width was 20cm (Fig 9c), tensile cracks initiate between the bolt and rock and propagate toward the model edge. In this configuration four tensile wing crack initiate from the tip of the indent and propagate

diagonally till coalescence with the bolt-rock interface. When cable width was 25cm (Fig 9d), tensile cracks initiate between the bolt and rock and propagate toward the model edge. In this configuration four tensile wing crack initiate from the tip of the indent and propagate diagonally till coalescence with the bolt-rock interface. When cable width was 30cm (Fig 9e),

tensile cracks initiate between the bolt and rock and propagate toward the model edge. In this configuration four tensile wing crack initiate from the tip of the indent and propagate diagonally till coalescence with the bolt-rock interface. Two rock wedges formed in this condition.
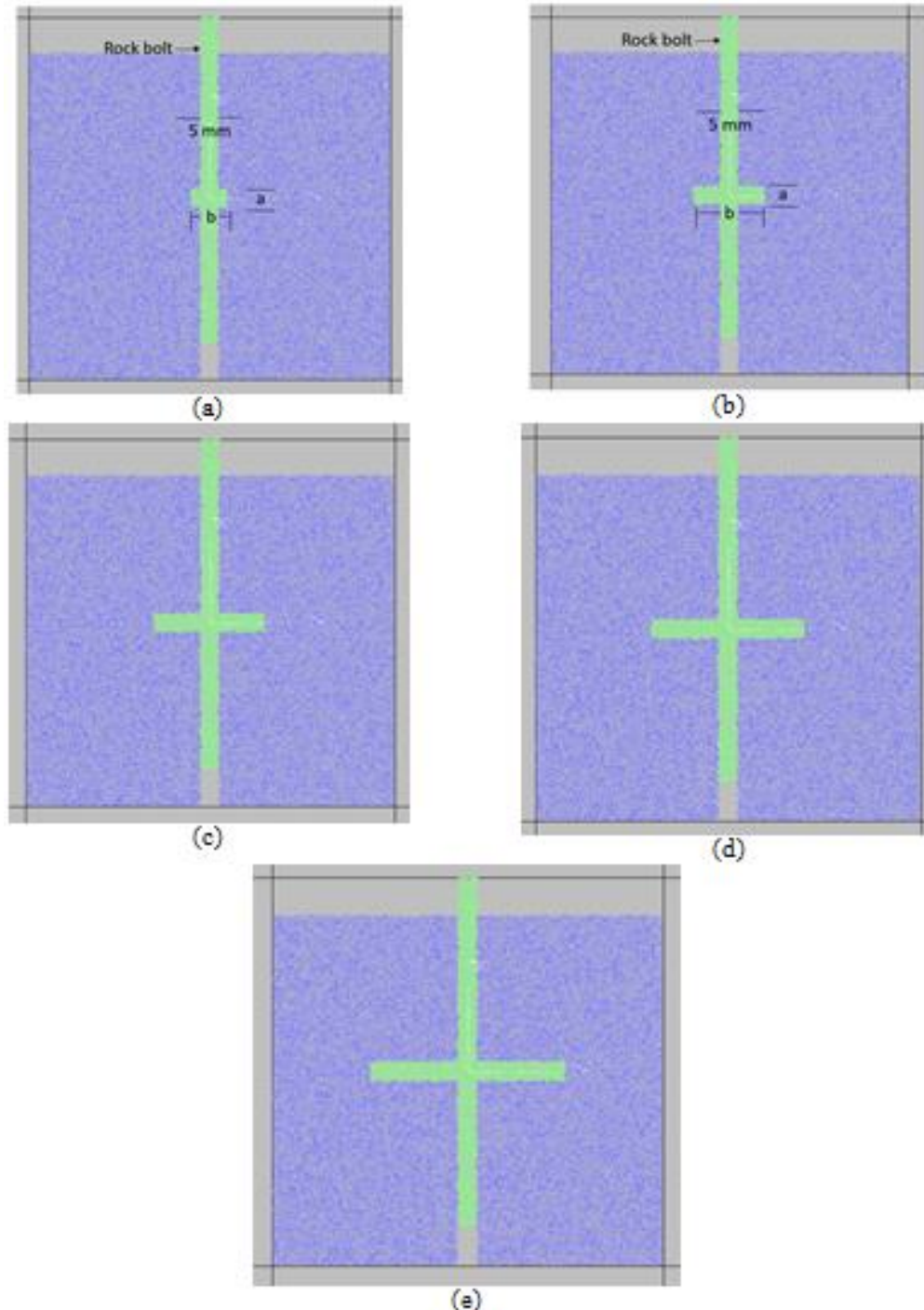

Figure 4. Numerical model with cable dimension of (a*b); a) 5cm*10cm b), 5cm*15cm c), 5cm*20 cm d), 5cm*25cm e), 5*30cm.
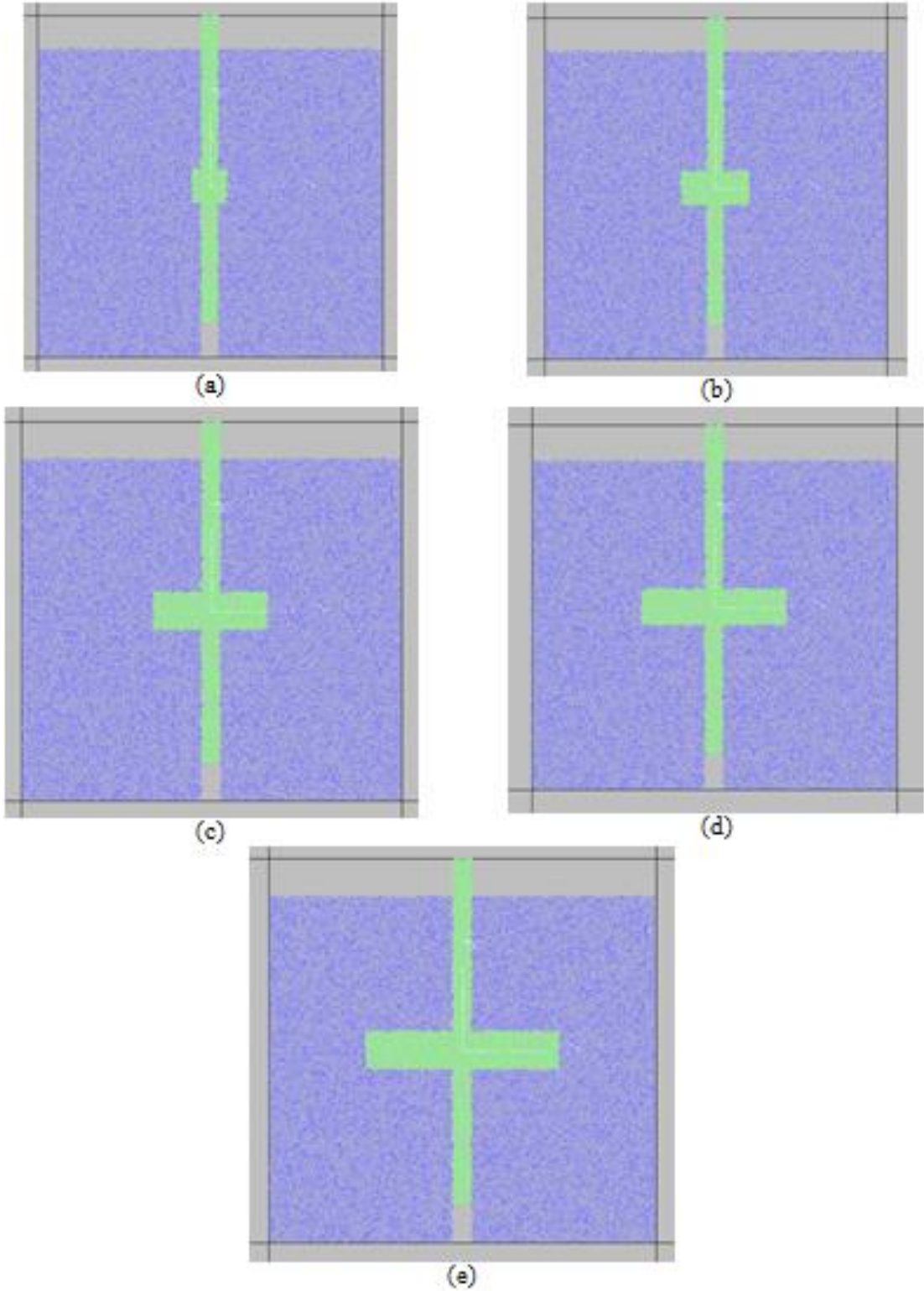
Figure 5. Numerical model with cable dimension of (a*b); a) 10cm*10cm b), 10cm*15cm c), 10cm*20 cm d), 10cm*25cm e), 10*30cm.
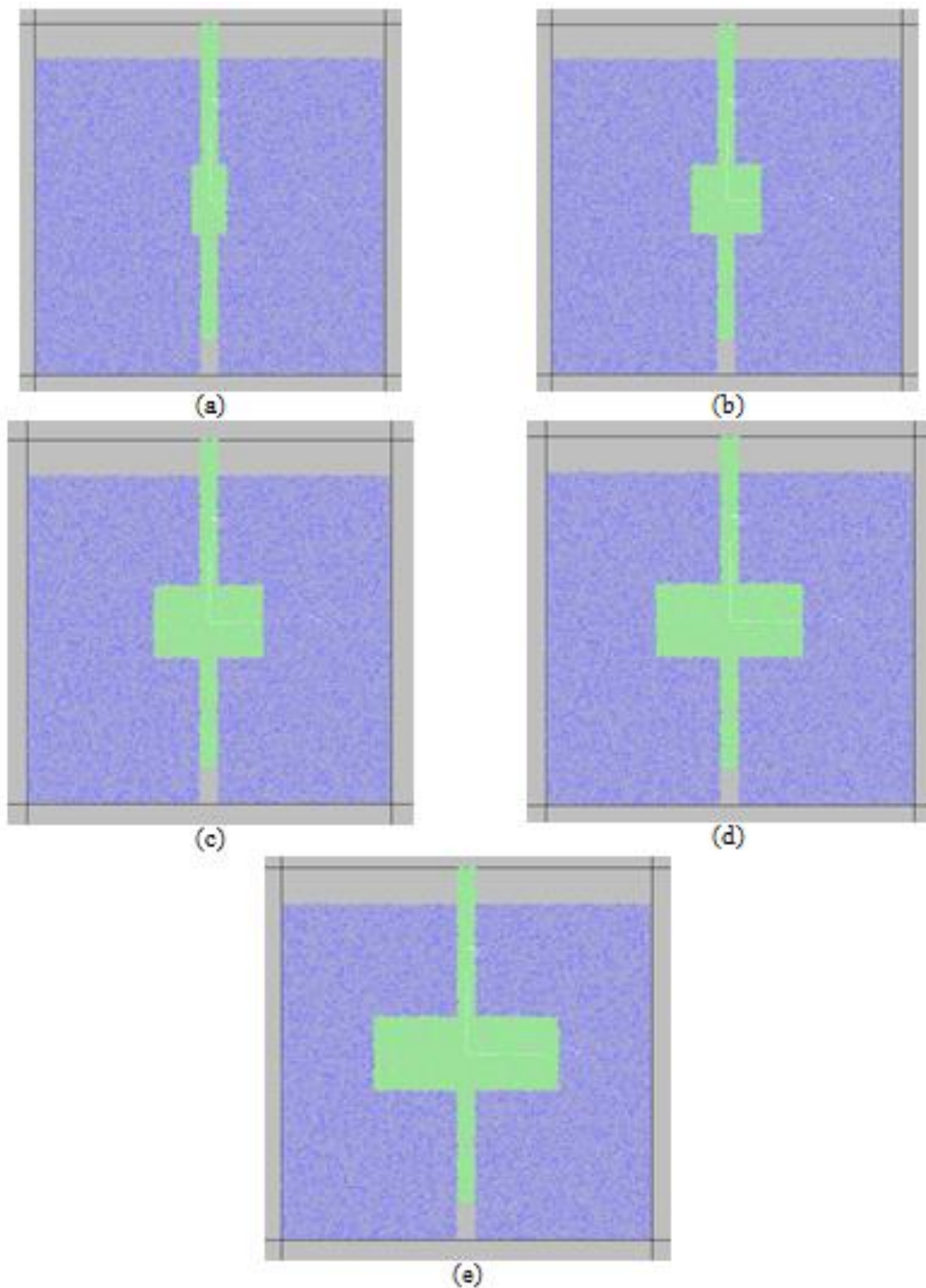
Figure 6. Numerical model with cable dimension of (a*b); a) 20cm*10cm b), 20cm*15cm c), 20cm*20 cm d), 20cm*25cm e), 20*30cm.
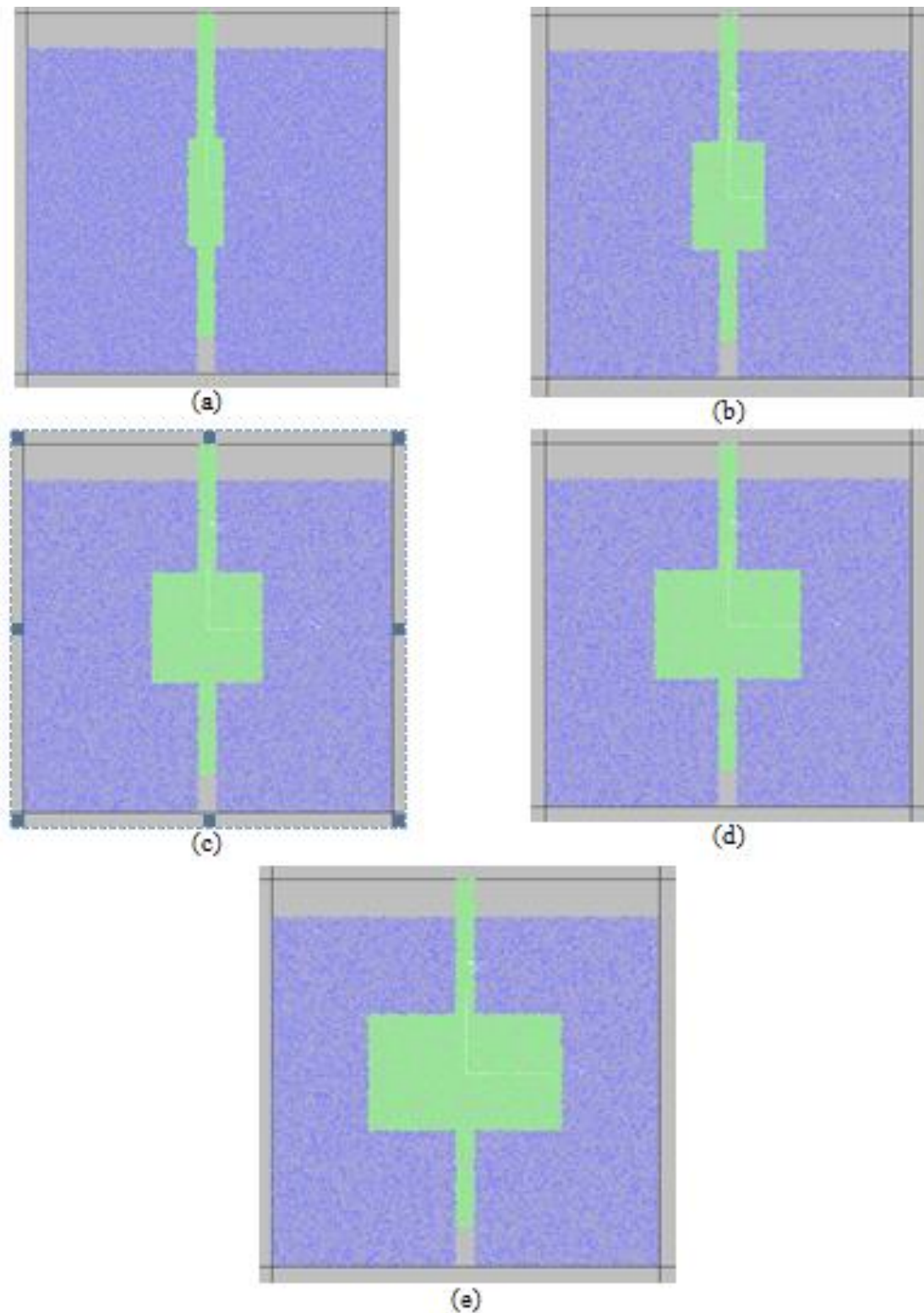
Figure 7. Numerical model with cable dimension of (a*b); a) 30cm*10cm b), 30cm*15cm c), 30cm*20 cm d), 30cm*25cm e), 30*30cm.

c)bolt length was 20 cm (a in Fig 4a):

When cable width was 10cm (Fig 10a), tensile cracks initiate between the bolt and rock and propagate toward the model edge. When cable width was 15cm (Fig 10b), tensile cracks initiate between the bolt and rock and propagate toward the model edge. In this configuration four tensile wing crack initiate from the tip of the indent and propagate diagonally till coalescence with the bolt-rock interface. When cable width was 20cm (Fig 10c), tensile cracks initiate between the bolt and rock and propagate toward the model edge. In this configuration four tensile wing crack initiate from the tip of the indent and propagate diagonally till coalescence with the bolt-rock

interface. When cable width was 25cm (Fig 10d), tensile cracks initiate between the bolt and rock and propagate toward the model edge. In this configuration four tensile wing crack initiate from the tip of the indent and propagate diagonally till coalescence with the bolt-rock interface. When cable width was 30cm (Fig 10e),

tensile cracks initiate between the bolt and rock and propagate toward the model edge. In this configuration four tensile wing crack initiate from the tip of the indent and propagate diagonally till coalescence with the bolt-rock interface. Two rock wedges formed in this condition.
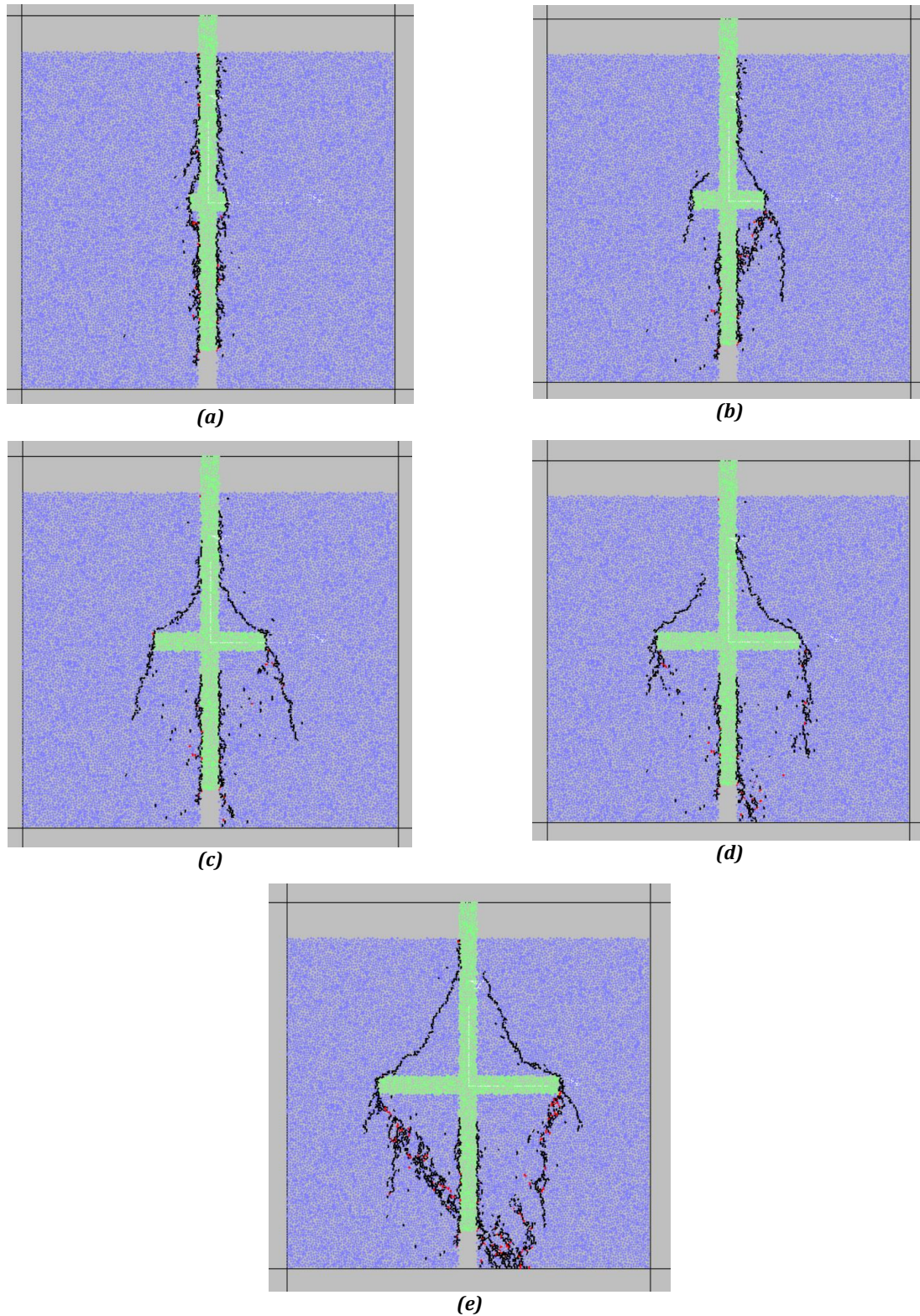

(a)

(b)

(c)

(d)

(e)

Figure 8. Failure pattern in numerical model with cable dimension of (a*b); a) 5cm*10cm b), 5cm*15cm c), 5cm*20 cm d), 5cm*25cm e), 5*30cm.
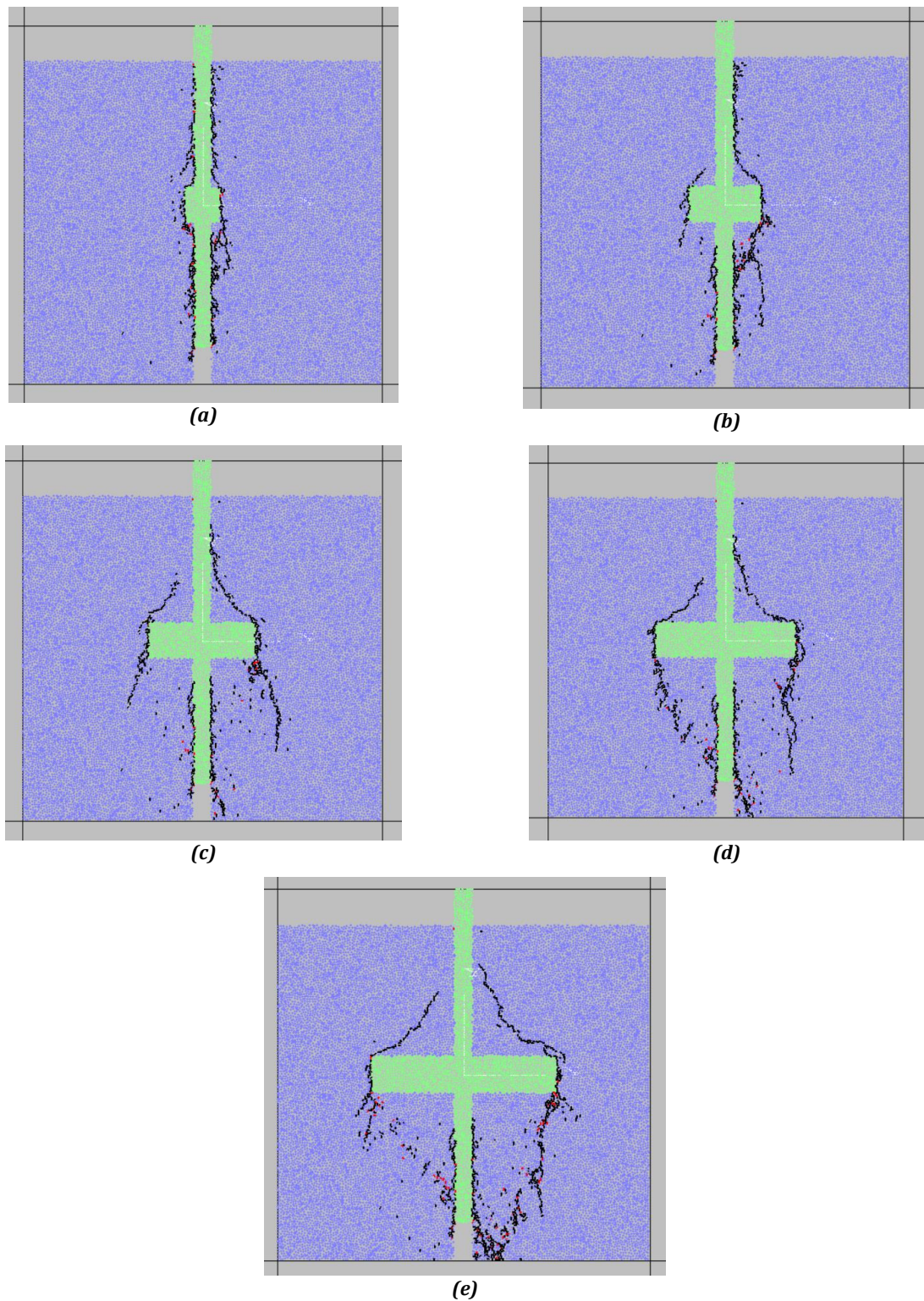
(a)

(b)

(c)

(d)

(e)

Figure 9. Failure pattern in numerical model with cable dimension of (a*b); a) 10cm*10cm b), 10cm*15cm c), 10cm*20 cm d), 10cm*25cm e), 10*30cm.

d)bolt length was 30 cm (a in Fig 4a):

When cable width was 10cm (Fig 11a), tensile cracks initiate between the bolt and rock and propagate toward the model edge. When cable width was 15cm (Fig 11b), tensile cracks initiate between the bolt and rock and propagate toward the model edge. In this configuration four tensile

wing crack initiate from the tip of the indent and propagate diagonally till coalescence with the bolt-rock interface. When cable width was 20cm (Fig 11c), tensile cracks initiate between the bolt and rock and propagate toward the model edge. In this configuration four tensile wing crack initiate from the tip of the indent and propagate diagonally till coalescence with the bolt-rock

interface. When cable width was 25cm (Fig 11d), tensile cracks initiate between the bolt and rock and propagate toward the model edge. In this configuration four tensile wing crack initiate from the tip of the indent and propagate diagonally till coalescence with the bolt-rock interface. When cable width was 30cm (Fig 11e),

tensile cracks initiate between the bolt and rock and propagate toward the model edge. In this configuration four tensile wing crack initiate from the tip of the indent and propagate diagonally till coalescence with the bolt-rock interface. Two rock wedges formed in this condition.
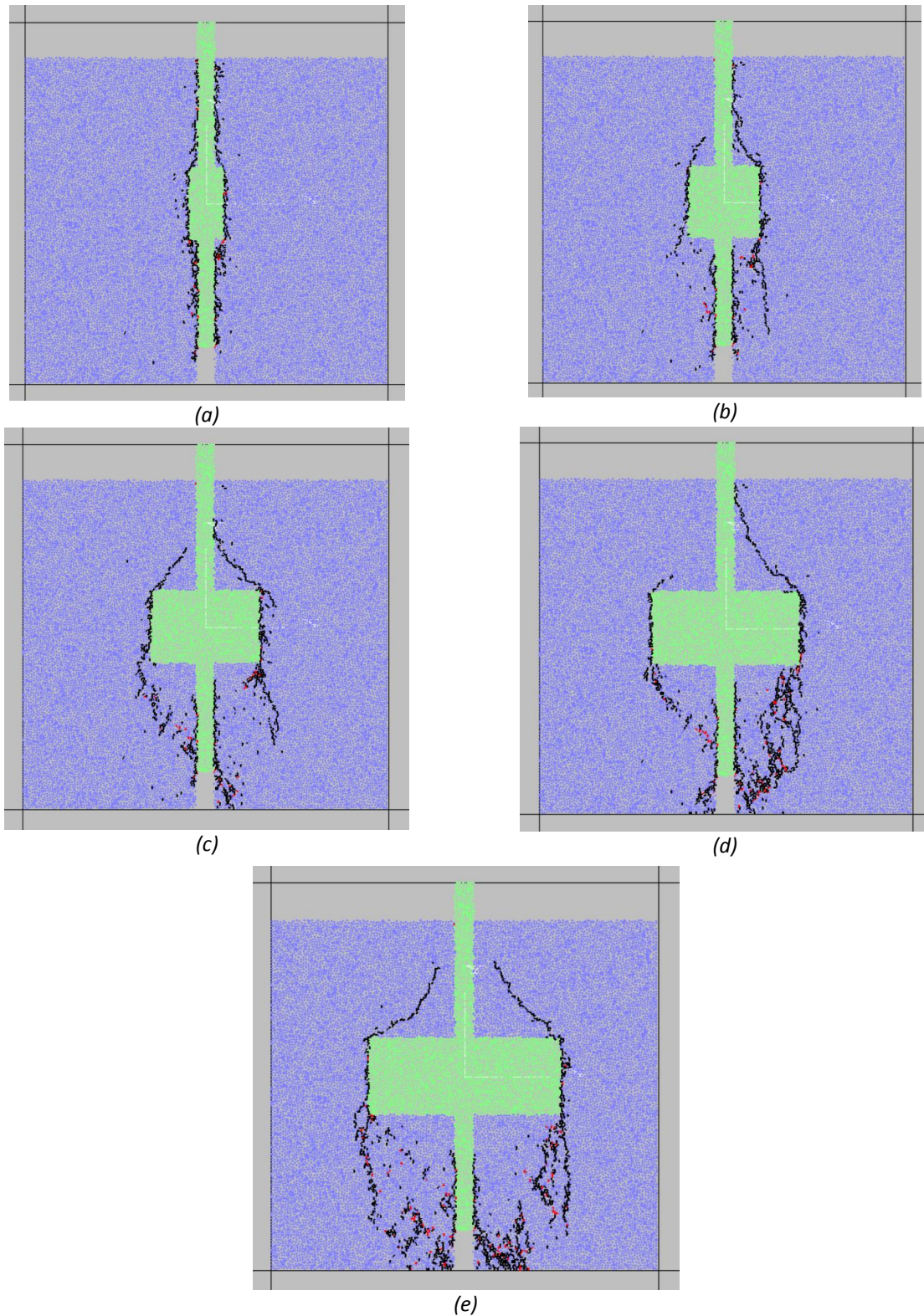

Figure 10. Failure pattern in numerical model with cable dimension of (a*b); a) 20cm*10cm b), 20cm*15cm c),20*20 cm d), 20cm*25cm e), 20*30cm.

(a)   *(b)*
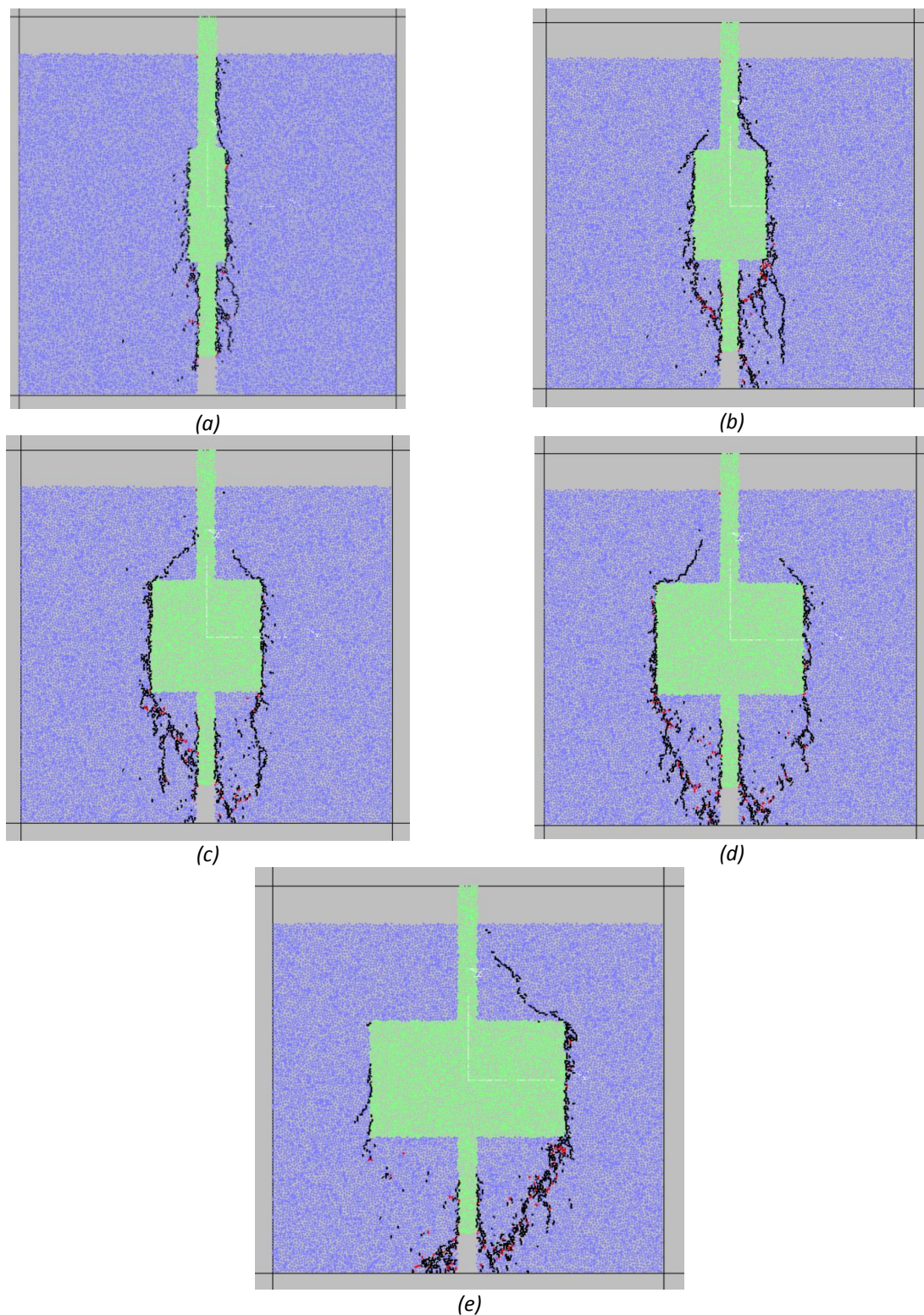

(c)   *(d)*

(e)

Figure 11. Failure pattern in numerical model with cable dimension of (a*b); a) 20cm*10cm b), 20cm*15cm c),20*20 cm d), 20cm*25cm e), 20*30cm.

4.2. The effect of cable indent dimension on the shear strength of the numerical model

Fig 12 shows the effect of cable indent dimension on the shear strength of the numerical model. The results of four cable indent length (a

in Fig 4a) has been depicted in this figure. The shear strength increased by increasing the cable indent width. Also, the shear strength increased by increasing the cable indent length.
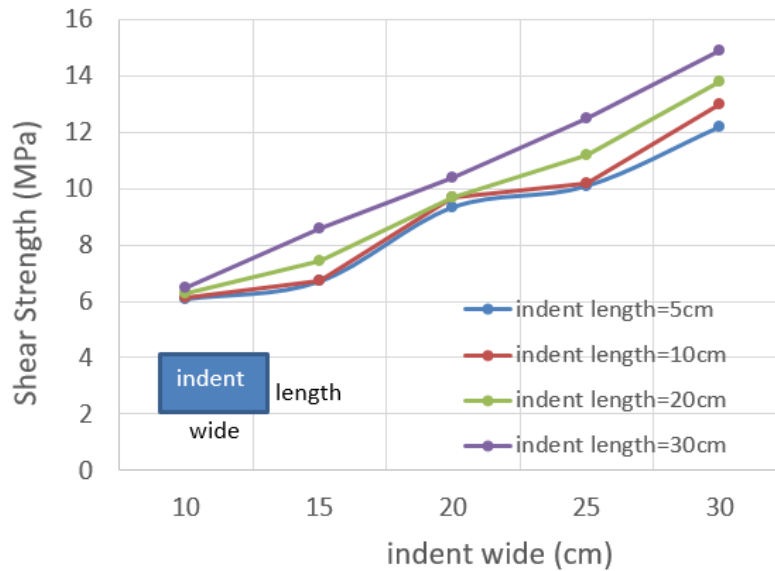
Figure 12. the effect of cable angle on the shear strength of the numerical model.

5. CONCLUSIONS

In this paper, the effect of cable indent shape on the shear behavior of rock-cable attachment surface has been investigated using PFC2D. Firstly, For this purpose, calibration of PFC was performed using the Brazilian experimental test and uniaxial compression test to reproduce the rock sample. Then, numerical models with a dimension of 100mm *100 mm were prepared. A cable with a different indent shape was inserted within the model. The punch shear test condition was added to the model. The normal load was fixed at 3.7 MPa (σc/10) and shear load was applied to the model till failure occurred. The results show that:

- When cable width was 10cm, tensile cracks initiate between the bolt and rock and propagate toward the model edge. When cable width was 15cm, tensile cracks initiate between the bolt and rock and propagate toward the model edge. In this configuration four tensile wing crack initiate from the tip of the indent and propagate diagonally till coalescence with the bolt-rock interface. This trend has occurred in different indent lengths.

- When cable width was 20cm, tensile cracks initiate between the bolt and rock and propagate toward the model edge. In this configuration four tensile wing crack initiate from the tip of the indent and propagate diagonally till coalescence with the bolt-rock interface. When cable width was 25cm, tensile cracks initiate between the bolt and rock and propagate toward the model edge. In this configuration four tensile wing crack initiate from the tip of the indent and propagate diagonally till coalescence with the bolt-rock

interface. This trend has occurred in different indent lengths.

- When cable width was 30cm, tensile cracks initiate between the bolt and rock and propagate toward the model edge. In this configuration four tensile wing crack initiate from the tip of the indent and propagate diagonally till coalescence with the bolt-rock interface. Two rock wedges formed in this condition. This trend has occurred in different indent lengths.

- The shear strength increased by increasing the cable indent width.

- The shear strength increased by increasing the cable indent length.

REFERENCES

[1] Stimpson, B. A simplified rock mass-rock bolt interaction analysis for horizontally layered strata. Geotech. Geol. Eng. 1991, 9, 27–51.

[2] Wang, G.; Han, W.; Jiang, Y.; Luan, H.; Wang, K. Coupling Analysis for Rock Mass Supported with CMC or CFC Rockbolts Based on Viscoelastic Method. Rock Mech. Rock Eng. 2019, 52, 4565–45883.

[3] Bjurström, S. Shear strength of hard rock joint hard rock joints reinforced by grouted untensioned bolts. In Proceedings of the Third Congress of the International Society for Rock Mechanics, Denver, CO, USA, 1–7 September 1974; pp. 1194–1199.

[4] Gerrard, C. Rock Bolting in Theory-A Keynote Lecture. In Proceedings of the International Symposium on Rock Bolting, Abisko, Sweden, 28

August–2 September 1983; A. A. Balkema: Rotterdam, The Netherlands, 1984; pp. 3–32.

[5] Spang, K.; Egger, P. Actionoffully-grouted bolts in jointed rock and factors of influence. Rock Mech. Rock Eng. 1990, 23, 201–229.

[6] Chen, N.; Zhang, X.; Jiang, Q.; Feng, X.; Wei, W.; Yi, B. Shear Behavior of Rough Rock Joints Reinforced by Bolts. Int. J. Geomech. 2018, 18, 04017130.

[7] Zhang, X.; Jiang, Q.; Kulatilake, P.; Xiong, F.; Yao, C. Influence of Asperity Morphology on Failure Characteristics and Shear Strength Properties of Rock Joints under Direct Shear Tests. Int. J. Geomech. 2018, 19, 04018196.

[8] Pellet, F.; Egger, P. Analytical model for the mechanical behaviour of bolted rock joints subjected to shearing. Rock Mech. Rock Eng. 1996, 29, 73–97.

[9] Ferrero, A.M. The shear strength of reinforced rock joints. Int. J.RockMech. Min. Sci. Geomech. Abstr. 1995, 32, 595–605.

[10] Liu, A.Q.; Ju, W.J. Analysis of Shear Resisting Action of Full-length Anchored Bolt with Pre-stress. Coal Min. Technol. 2012, 17, 45–48.

[11] Selvadurai, A.P.S.; Yu, Q. Mechanics of a discontinuity in a geomaterial. Comput. Geotech. 2005, 32, 92–106.

[12] Bahaaddini, M.; Sharrock, G.; Hebblewhite, B.K. Numerical direct shear tests to model the shear behaviour of rock joints. Comput. Geothech. 2013, 51, 101–115.

[13] Zhou, Y.; Misra, A.; Shunchuan, W.U.; Zhang, X. Macro-and meso-analyses of rock joint direct shear test using particle flow thory. Chin. J. Rock Mech. Eng. 2012, 31, 1245–1256.

[14] H.C.Andrade, E.D.Leone, An enriched dual boundary element method formulation for linear elastic crack propagation, Engineering Analysis with Boundary Elements, Volume 121, December 2020, Pages 158-179.

[15] Alexander H.-D. Cheng Emmanuel Detournay, A direct boundary element method for plane strain poroelasticity, International Journal for Numerical and Analytical Methods in Geomechanics, vol. 12, issue 5, pp. 551-572. 1988.

[16] MF Marji, H Hosseini-Nasab, AH Kohsary, A new cubic element formulation of the displacement discontinuity method using three special crack tip elements for crack analysis, JP J. Solids Struct 1 (1), 61-91, 2007.

[17] M Behnia, K Goshtasbi, MF Marji, A Golshani, Numerical simulation of crack propagation in layered formations, Arabian Journal of Geosciences 7 (7), 2729-2737, 2014. In this paper, the finite difference and discrete element methods are used to simulate the shear behavior of rock-rock bolt interface.

[18] Park, J.W.; Song,J.J. Numerical simulation of a direct shear test on a rock joint using abonded-particle model. Int. J. Rock Mech. Min. Sci. 2009, 46, 1315–1328.

[19] Zhao, T.B.; Yin, Y.C.; Tan, Y.L.; Qiu, Y. Mechanical Test of Bolt Interface and Microscopic Simulation of Transfer Law for Shear Stress. J. Min. Saf. Eng. 2011, 28, 220–224.

[20] Dugdale, D.S. Yielding of steel sheets containing slits. J. Mech. Phys. Solids 1960, 8, 100–104.

[21] Barenblatt, G.I. The Mathematical Theory of Equilibrium Cracks in Brittle Fracture. Adv. Appl. Mech. 1962, 7, 55–129.

[22] Qiao, P.; Chen, Y. Cohesive fracture simulation and failure modes of FRP–concrete bonded interfaces. Theor. Appl. Fract. Mech. 2008, 49, 213–225.

[23] Hawileh, R.A.; Naser, M.Z.; Abdalla, J.A. Finite element simulation of reinforced concrete beams externally strengthened with short-length CFRP plates. Compos. Part B Eng. 2013, 45, 1722–1730.

[24] Cameselle-Molares, A.; Vassilopoulos, A.P.; Renart, J.; Turon, A.; Keller, T. Numerical simulation of two-dimensional in-plane crack propagation in FRP laminates. Compos. Struct. 2018, 200, 396–407.

[25] Su,X.T.; Yang,Z.J.; Liu,G.H. Monte Carlo simulation of complex cohesive fracture in random heterogeneous quasi-brittle materials: A 3D study. Int. J. Solids Struct. 2010, 47, 2336–2345.

[26] Bahaaddini, M., Sharrock, G., Hebblewhite, B. K. "Numerical investigation of the effect of joint geometrical parameters on the mechanical properties of a non-persistent jointed rock mass under uniaxial compression." Computers and Geotechnics. 49, pp. 206–225. 2013.

[27] D. O. Potyondy and P. A. Cundall, "A bonded-particle model for rock," International Journal of Rock Mechanics and Mining Sciences, vol.41, no.8, pp.1329–1364, 2004.

[28] Ghazvinian, A., Sarfarazi, V., Schubert, W. and Blumel, M. (2012), "A study of the failure mechanism of planar non-persistent open joints using PFC2D", Rock Mech. Rock Eng., 45(5), 677-693.